SOLAR CELLS

Engineering ligand reactivity enables high-temperature operation of stable perovskite solar cells

So Min Park[1]†, Mingyang Wei[2]†, Jian Xu[1]†, Harindi R. Atapattu[3], Felix T. Eickemeyer[2], Kasra Darabi[4], Luke Grater[1], Yi Yang[5], Cheng Liu[5], Sam Teale[1], Bin Chen[1,5], Hao Chen[1], Tonghui Wang[4], Lewei Zeng[1], Aidan Maxwell[1], Zaiwei Wang[1], Keerthan R. Rao[3], Zhuoyun Cai[6], Shaik M. Zakeeruddin[2], Jonathan T. Pham[6], Chad M. Risko[6], Aram Amassian[4], Mercouri G. Kanatzidis[5], Kenneth R. Graham[3]*, Michael Grätzel[2]*, Edward H. Sargent[1,5,7]*

Perovskite solar cells (PSCs) consisting of interfacial two- and three-dimensional heterostructures that incorporate ammonium ligand intercalation have enabled rapid progress toward the goal of uniting performance with stability. However, as the field continues to seek ever-higher durability, additional tools that avoid progressive ligand intercalation are needed to minimize degradation at high temperatures. We used ammonium ligands that are nonreactive with the bulk of perovskites and investigated a library that varies ligand molecular structure systematically. We found that fluorinated aniliniums offer interfacial passivation and simultaneously minimize reactivity with perovskites. Using this approach, we report a certified quasi–steady-state power-conversion efficiency of 24.09% for inverted-structure PSCs. In an encapsulated device operating at 85°C and 50% relative humidity, we document a 1560-hour T_{85} at maximum power point under 1-sun illumination.

M etal-halide perovskite solar cells (PSCs) are emerging photovoltaic (PV) technologies that hold promise in terawatt-scale deployment (1). They unite high power-conversion efficiencies (certified PCEs up to 25.7%) (2) with low-cost solution processing that uses abundant materials (3–5). To compete with crystalline silicon (c-Si) solar cells and to be applied with c-Si in tandem cells, PSCs will need improved evidence of bankability (6), such as operating stability at elevated temperatures in accelerated aging (7–12).

Interfaces, which have high defect densities (13, 14) and low barriers to ion transfer (15, 16) and are susceptible to moisture- and oxygen-induced degradation (17, 18), can provide pathways for energy loss and degradation in PSCs (19, 20). In record-efficiency PSCs, interfaces have been passivated by using two- and three-dimensional (2D/3D) hybrid structures (21–23), where a thin layer of Ruddlesden-Popper 2D perovskites terminates the 3D-perovskite surface. These 2D/3D structures are constructed by exposing perovskite surfaces to a solution containing ammonium ligands, during which the 3D lattice is fragmented into 2D layers (24, 25). This approach is beneficial because the 2D overlayer increases the resistance of perovskites to degradation (17, 26).

There is a diversity of findings in reports on the stability of 2D overlayers under stress. Some studies have indicated limited stability of the 2D/3D interface under thermal stress (27–29). Progress has been made, with a recent study demonstrating 500-hour operating stability under conditions of 65°C, 50% relative humidity (RH), and maximum power point (MPP) tracking [International Summit on Organic Photovoltaic Stability (ISOS)-L-3-65°C], enhanced by the incorporation of 3-fluorophenethylammonium (3FPEA) intercalation (23). Another study (30) that used an oleylammonium-intercalated 2D overlayer showed promising results in a 1000-hour damp-heat test, although this study was based on silicon PV module IEC 61215:2016 standards (85°C and 85% RH, dark).

Given these promising performance and stability improvements, the field continues to pursue ever-higher durability targets. There is interest in raising the standard to 85°C ISOS-L-3 (MPP tracking at 85°C and 50% RH). However, the reactivity of ammonium ligands with 3D perovskites may lead to further penetration into the bulk perovskite film (28, 31, 32) and may contribute to deterioration in device performance under these very demanding stress conditions (27, 28, 31–33). Thus, we explored noninvasive surface-passivating ligands, but we did note that in prior studies, these have yet to achieve the remarkable benefits of the 2D/3D strategy.

We sought to understand how molecular structure affects ligand reactivity with 3D perovskites. Previous studies used bulkier ammonium ligands to suppress ligand intercalation, whereas certain small-sized ammonium ligands exhibit low reactivity (34, 35). We attribute this difference to the limited availability of characterization techniques that allow one to compare ligand reactivity among different ammonium molecules—a particularly challenging pursuit in view of the ultrathin nature (typically <10 nm) of the passivating overlayer (23).

Spectroscopy studies of ammonium ligands in perovskites

We used angle-resolved x-ray photoelectron spectroscopy (AR-XPS) and time-of-flight secondary ion mass spectrometry (TOF-SIMS) to investigate the penetration of a library of ammonium ligands into the bulk of perovskites (Fig. 1A), which include varying tail groups and alkyl chain lengths. A small-sized ammonium ligand, anilinium (An), had the lowest reactivity with 3D perovskites. We then explored derivatives of An with different degrees of fluorination to couple low ligand reactivity with effectual interfacial passivation. These molecules improved operating stability for the encapsulated PSC at 85°C and 50% RH.

Ammonium ligands were deposited on $Cs_{0.05}MA_{0.05}FA_{0.9}Pb(I_{0.95}Br_{0.05})_3$ perovskite films (materials and methods), and films were annealed at 100°C (31). We used AR-XPS to probe the spatial distribution of ammonium ligands in the out-of-plane direction (Fig. 1B). AR-XPS is a nondestructive depth-profiling technique used to determine the composition of ultrathin layers (<10 nm) at the top surfaces of films (36, 37). We varied the probe depth by changing the angle between the normal of the perovskite sample and the analyzer. Three different electron takeoff angles (0°, 45°, and 75°) were selected, with probe depths varying from ~6 to 8 nm at 0° to ~1 to 2 nm at 75° (Fig. 1C).

To obtain the proportion of ammonium ligands at a given probe depth, we compared the ratio of C-N, where N signals originated from methylammonium (MA) and ammonium ligands at a binding energy of ~401.5 eV, with the N signals originating from formamidinium (FA) at a binding energy of ~399.8 eV in the peak area in the N 1s XPS spectrum (figs. S1 and S2). The C-N/FA N ratio plots (Fig. 1D) revealed that the aryl ammoniums phenethyl-ammonium (PEA) and 3FPEA had relatively uniform depth distributions. By contrast, alkyl ammoniums butylammonium (BA) and octyl-ammonium (OA) tended to accumulate on the top surfaces, as evidenced by the C-N/FA N ratio increasing with larger electron takeoff angles. However, each of the ligands yielded C-N/FA N ratios greater than those of untreated perovskites (control) for all electron

[1]Department of Electrical and Computer Engineering, University of Toronto, 10 King's College Road, Toronto, Ontario M5S 3G4, Canada. [2]Laboratory of Photonics and Interfaces, Ecole Polytechnique Fédérale de Lausanne, 1015 Lausanne, Switzerland. [3]Department of Chemistry, University of Kentucky, Lexington, KY 40506, USA. [4]Department of Materials Science and Engineering, and Organic and Carbon Electronics Laboratories (ORaCEL), North Carolina State University, Raleigh, NC 27695, USA. [5]Department of Chemistry, Northwestern University, Evanston, IL 60208, USA. [6]Department of Chemical and Materials Engineering, University of Kentucky, Lexington, KY 40506, USA. [7]Department of Electrical and Computer Engineering, Northwestern University, Evanston, IL 60208, USA.
†These authors contributed equally to this work.
*Corresponding author. Email: ted.sargent@utoronto.ca (E.H.S.); michael.graetzel@epfl.ch (M.G.); kenneth.graham@uky.edu (K.R.G.)

takeoff angles (Fig. 1E), indicating their distinct contributions to C-N signals and their intercalation into the bulk of perovskites.

We then examined long-chain alkyl ammonium decylammonium (DA), along with small-sized An (34, 35, 38). For DA, the C-N/FA N ratio decreased with a larger electron takeoff angle (Fig. 1D). The reversed trend, as compared with other alkyl ammoniums, suggested that DA molecules diffused into the bulk of perovskites. By contrast, An exhibited low reactivity and had limited penetration into perovskites. The C-N/FA N ratios for An were a factor of ~2 less than those for PEA at different electron takeoff angles and are similar to control perovskites (Fig. 1E).

At these low C-N/FA N ratios, quantifying the extent of ligand penetration was difficult, given the prominent C-N contribution from MA cations (fig. S2 and table S1). We thereby performed TOF-SIMS and found that, whereas PEA cations were distributed throughout the thickness of the perovskite film, An cations were detected only at the top surface of the film (fig. S3). The combination of AR-XPS and TOF-SIMS supported An remaining surface localized.

Although An exhibited low ligand reactivity, it has also been reported to have limited passivating capacity (35, 39). To promote interfacial passivation, we explored fluorinated An, including 4-fluoroanilinium (4FAn), 2,6-difluoroanilinium (26FAn), and 3,4,5-trifluoroanilinium (345FAn), as well as tert-butyl-substituted 3,5-di-tert-butylanilinium (35tbuAn) (17, 40, 41). The C-N/FA N ratios (Fig. 1E) revealed that, compared with An, the newly synthesized ligands retained similarly low reactivity with perovskites. For fluorinated An, this low reactivity was also seen in the C-F signal in the F 1s XPS spectrum (fig. S4). We identified a distinct C-F peak for 3FPEA, whereas the C-F signals from 4FAn, 26FAn, and 345FAn were all below the detection limit at the different electron takeoff angles. TOF-SIMS further confirmed that 345FAn cations were localized to the surface of the perovskite film (fig. S5).

We then characterized the phase transformation of perovskites driven by their interaction with ammonium ligands. Ultrafast transient reflection (TR) spectroscopy was used initially to detect 2D perovskite formation (42). For the PEA-treated perovskite films, negative reflectance features associated with

n = 1, 2, and 3 layered 2D perovskites were observed in the TR spectra (Fig. 2A). The relative proportion of 2D phases increased as the solution exposure time was prolonged (fig. S6) and was indicative of progressive phase transformation. For the An- and 345FAn-treated perovskite films, no 2D phases were observed (Fig. 2, B and C), which we attributed to their inability to convert 3D perovskites into 2D phases (fig. S7). These results reinforce the model proposing that inhibiting 2D phase conversion would also reduce ligand penetration.

We also investigated phase transformation with grazing incidence wide-angle x-ray scattering (GIWAXS) measurements. Consistent with the TR studies, n = 2 2D perovskites were observed at around q = 0.29 Å^{-1} along q_z for the PEA-treated perovskite film (Fig. 2D) that blocks vertical carrier transport (32). Incidence angle–dependent diffraction patterns of PEA-treated perovskites revealed that the 2D phase formation was more pronounced near the surface (fig. S8). No 2D phase was detected in the An- and 345FAn-treated perovskites (Fig. 2, E and F).

In addition, we observed the formation of PbI$_2$ at q = 0.9 Å^{-1} for An-treated perovskite films,

Fig. 1. AR-XPS characterization of ammonium ligand penetration. (**A**) Chemical structures of the ammonium ligands investigated in this study. (**B**) Experimental setup for AR-XPS characterization. The electron takeoff angle α is defined as the angle between the normal of the sample substrate and the analyzer. (**C**) Schematic indicating the relation between α and the photoelectron probing depth, d. (**D** and **E**) C-N to FA N ratios at electron takeoff angles of 0°, 45°, and 75° for the control (untreated) and ammonium ligand–treated perovskite films. The results show reduced bulk and surface existence for An and An derivatives.
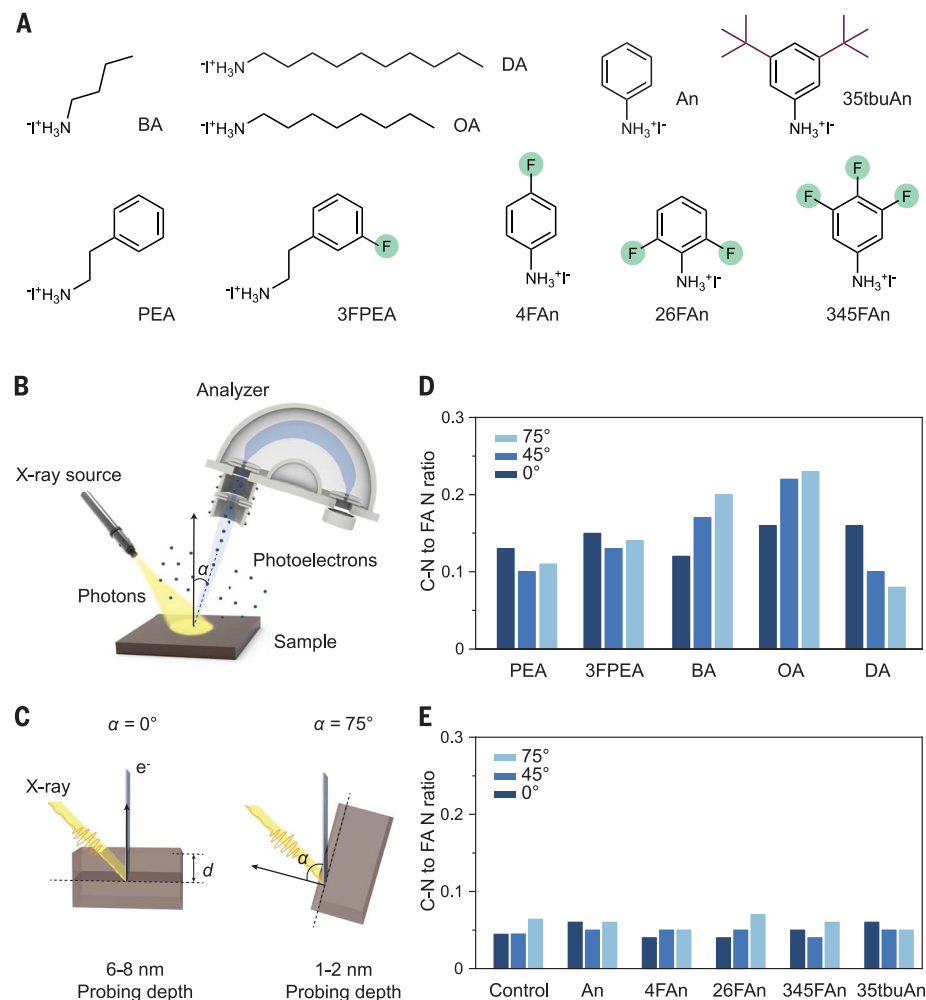
which we attributed to polar solvent–induced decomposition during solution exposure, as seen in x-ray diffraction (XRD) characterization (fig. S9). This is a topic that requires further in-depth investigation. GIWAXS characterization showed that 345FAn protected the underlying perovskites from this solvent-induced degradation (Fig. 2F). We associate the reduction in surface degradation with increased hydrophobicity of this fluorinated ligand (fig. S10) (26).

Theoretical calculations

The interactions of ammonium ligands and perovskites are depicted in Fig. 3A. We performed density functional theory (DFT) calculations to explore how molecular structure affected these interactions. We first calculated the binding energies (E_b) of two adjacent perovskite fragments at their interface with the insertion of ammonium ligands (Fig. 3B). A more negative E_b implies that it is thermodynamically more favorable to form the 2D/3D heterostructures (24). Consistent with the AR-XPS studies, penetrating PEA had a more negative E_b value than alkyl ammoniums OA and BA, whereas An and its derivatives showed the least tendency to form 2D/3D structures (Fig. 3C).

It has been suggested that the formation of 2D perovskites is related to the steric hindrance around the NH_3^+ group (43). We calculated the steric effect index (STEI, defined as the steric environment around the NH_3^+ group) of the ammonium ligand (43) and found that An had a much larger STEI (2.34) than that of PEA (1.21). Furthermore, phase transformation entailed the replacement of A-site cations at 2D/3D interfaces (24). DFT calculations indicated that this process demanded more energy for An-intercalated interfaces than for PEA-intercalated ones (fig. S11). This evidence further supported our finding that An was less likely to penetrate the bulk of perovskites through ligand intercalation.

We proceeded to examine the interactions between ammonium ligands and perovskite surfaces. We calculated the interaction energy (E_{int}) for the scenario in which an ammonium ligand occupied an MA-vacancy site on the perovskite surface (Fig. 3D). Electrostatic potential calculations showed that fluorine substitution resulted in a higher positive charge density near the ammonium group (fig. S12) that could enhance its binding with the negatively charged MA vacancy (13). Indeed, the E_{int} values were −0.74, −0.89, −0.92, and −1.22 eV for An, 4FAn, 26FAn, 345FAn, respectively (Fig. 3E), indicating that 345FAn exhibited the strongest interaction with the perovskite surface. Future computational studies could beneficially predict the binding energy of the N 1s XPS peak.

Perovskite degradation and solar cell studies

We used TR and TOF-SIMS to study perovskite degradation. The TR results indicated that PEA-based 2D perovskites were thermally unstable on the film surface and decomposed into PbI_2 after thermal aging at 85°C for 2 hours (Fig. 4, A and B). This process we associated with the diffusion of PEA cations into bulk perovskites,
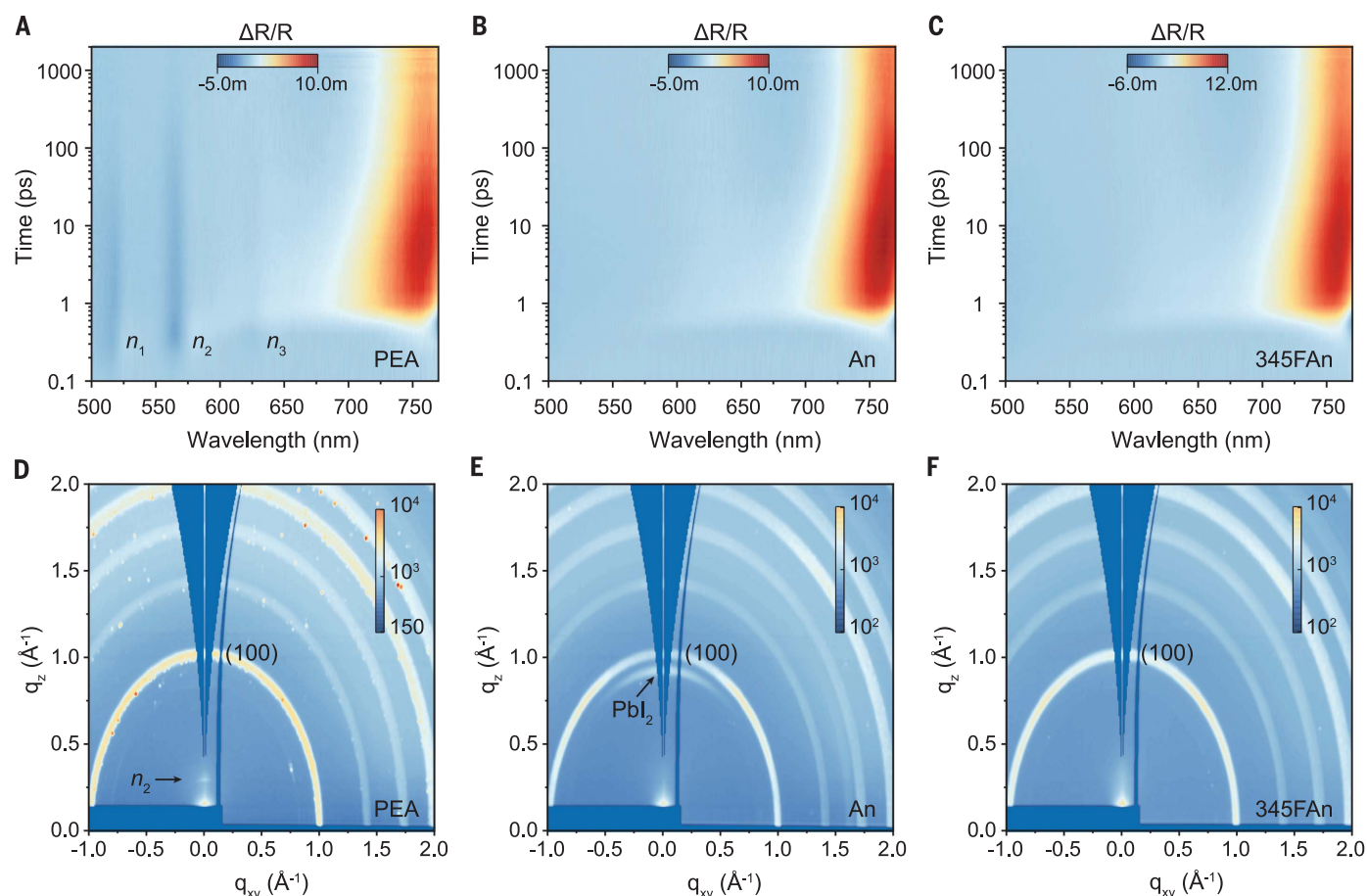
Fig. 2. Phase transformation of perovskite films. (**A** to **C**) Pseudocolor representation of the transient reflectance spectra, $\Delta R/R$, for the PEA- (A), An- (B), and 345Fan-treated (C) perovskite films, respectively. n = 1, n = 2, n = 3 2D perovskites (n_1, n_2, and n_3) appear in the film after PEA passivation. (**D** to **F**) GIWAXS image for perovskite films of PEA (D), An (E), and 345FAn (F) passivation, respectively. The color bar shows the diffraction intensity collected from the GIWAXS detector. q_{xy} and q_z represent in-plane and near out-of-plane scattering vectors, respectively. n = 2 2D perovskite (n_2) and PbI_2-related diffraction peaks are observed in the PEA- and An-treated films, respectively. (100) refers to the (100) diffraction peak of 3D perovskites.

Fig. 3. DFT studies.
(**A**) Schematic depiction of the model of ammonium ligand and perovskite interactions. (**B**) Models used in DFT calculations to calculate the binding energy (E_b) of adjacent 2D perovskite fragments. (**C**) E_b values for seven ammonium ligands substituted into MAPbI$_3$ perovskite slabs. (**D**) Models used to calculate the interaction energy (E_{int}) of ammonium ligands with the MAPbI$_3$ perovskite surface. (**E**) E_{int} values of four ammonium ligands with the perovskite surface.
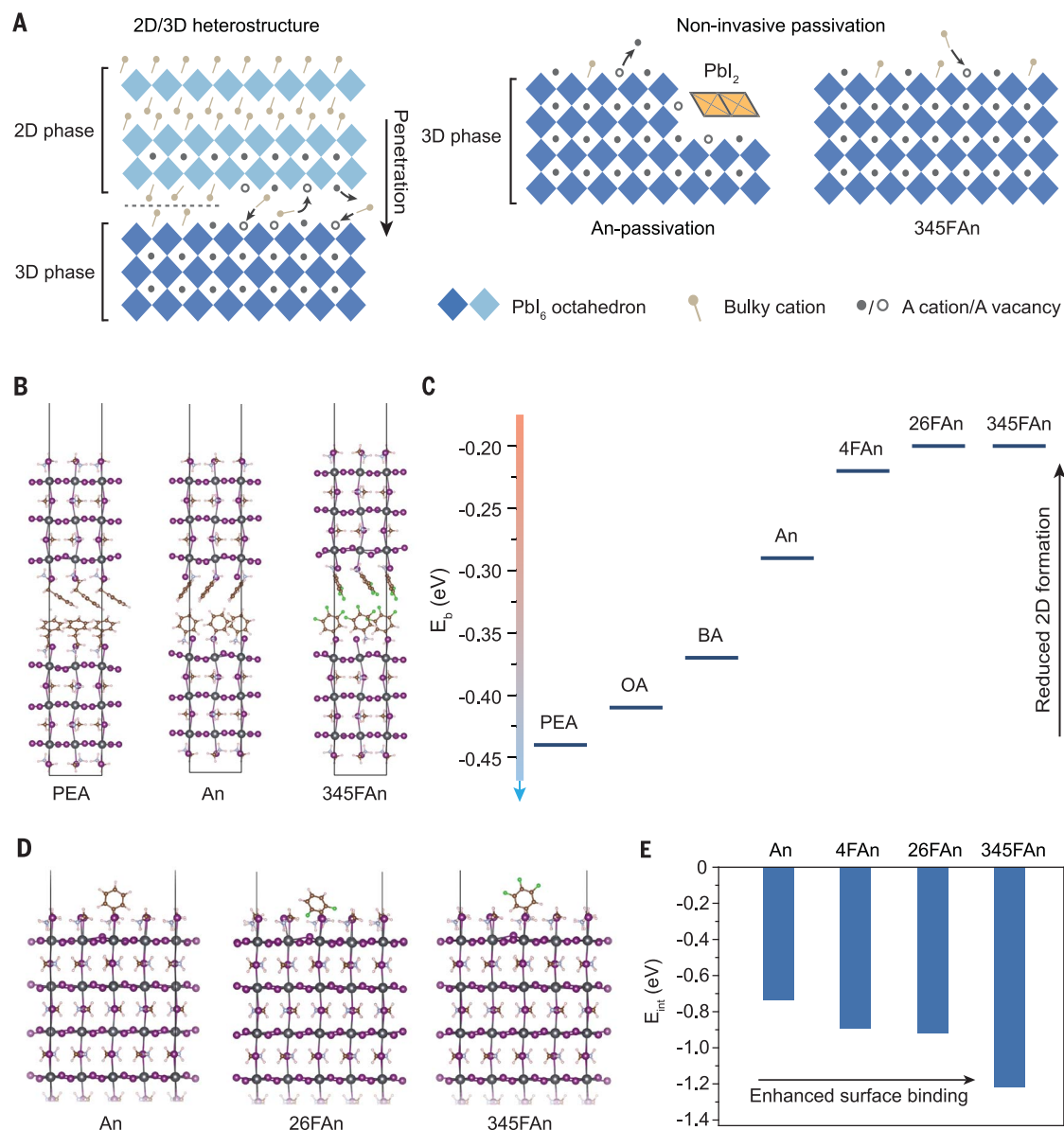
as was seen with TOF-SIMS (Fig. 4C) and AR-XPS (fig. S13). The dynamic nature of 2D/3D heterostructures was also confirmed for BA, OA, DA, and 3FPEA (fig. S14). By contrast, neither ligand penetration nor phase degradation was observed for An- and 345FAn-treated films (Fig. 4C and fig. S15). These results suggested that suppressing ligand intercalation into 3D perovskites improved interface stability under thermal stress.

We monitored the photoluminescence (PL) stability of perovskite films after annealing at 85°C (Fig. 4D). The emission intensity of the untreated control and PEA-treated films degraded to 30% of its initial value within 144 hours (Fig. 4E), as seen in the previous reports (*31*). By contrast, An- and 345FAn-treated films show improved thermal stability, and 345FAn-treated perovskites retained 85% of their initial brightness after annealing.

We fabricated inverted-structure PSCs to investigate how ammonium ligands influenced the efficiency and stability of PSCs. We used both Cs$_{0.05}$MA$_{0.05}$FA$_{0.9}$Pb(I$_{0.95}$Br$_{0.05}$)$_3$ and Cs$_{0.05}$MA$_{0.15}$FA$_{0.8}$PbI$_3$ perovskites as the absorber, the self-assembled monolayer 2PACz as the hole transport layer, the thermally evaporated C$_{60}$/bathocuproine (BCP) bilayer as the electron transport layer, and indium tin oxide (ITO) as the transparent electrode (materials and methods). Three representative ammonium ligands, including the 2D-forming PEA cation and the noninvasive An and 345FAn cations, were used for interfacial engineering. The cross-sectional scanning electron microscope (SEM) image of a complete device is shown in fig. S16.

Device performance (Fig. 5A) showed that compared with control devices, PEA-treated Cs$_{0.05}$MA$_{0.15}$FA$_{0.8}$PbI$_3$ PSCs (16 devices) pro-

vided improved PV performance with an average PCE of 23.2% (Fig. 5A and fig. S17). The average PCE of An devices decreased to 19.9%, a finding we linked to perovskite decomposition. Because of the improved surface passivation, 345FAn treatment increased average PCEs of Cs$_{0.05}$MA$_{0.15}$FA$_{0.8}$PbI$_3$ and Cs$_{0.05}$MA$_{0.05}$FA$_{0.9}$Pb(I$_{0.95}$Br$_{0.05}$)$_3$ PSCs to 23.3 and 22.9%, respectively (Fig. 5A and fig. S18). The external quantum efficiency (EQE) spectra of the champion cells (Fig. 5B) for PEA and 345FAn devices exhibited improved charge collection compared with controls, and their integrated short-circuit current density (J_{sc}) values matched well with those from the current-voltage (I-V) sweep.

We sent a 345FAn-treated Cs$_{0.05}$MA$_{0.15}$FA$_{0.8}$PbI$_3$ device to National Renewable Energy Laboratory (NREL, USA) for independent characterization. The device delivered a certified PCE of 24.09% by using a quasi–steady-state (QSS) I-V
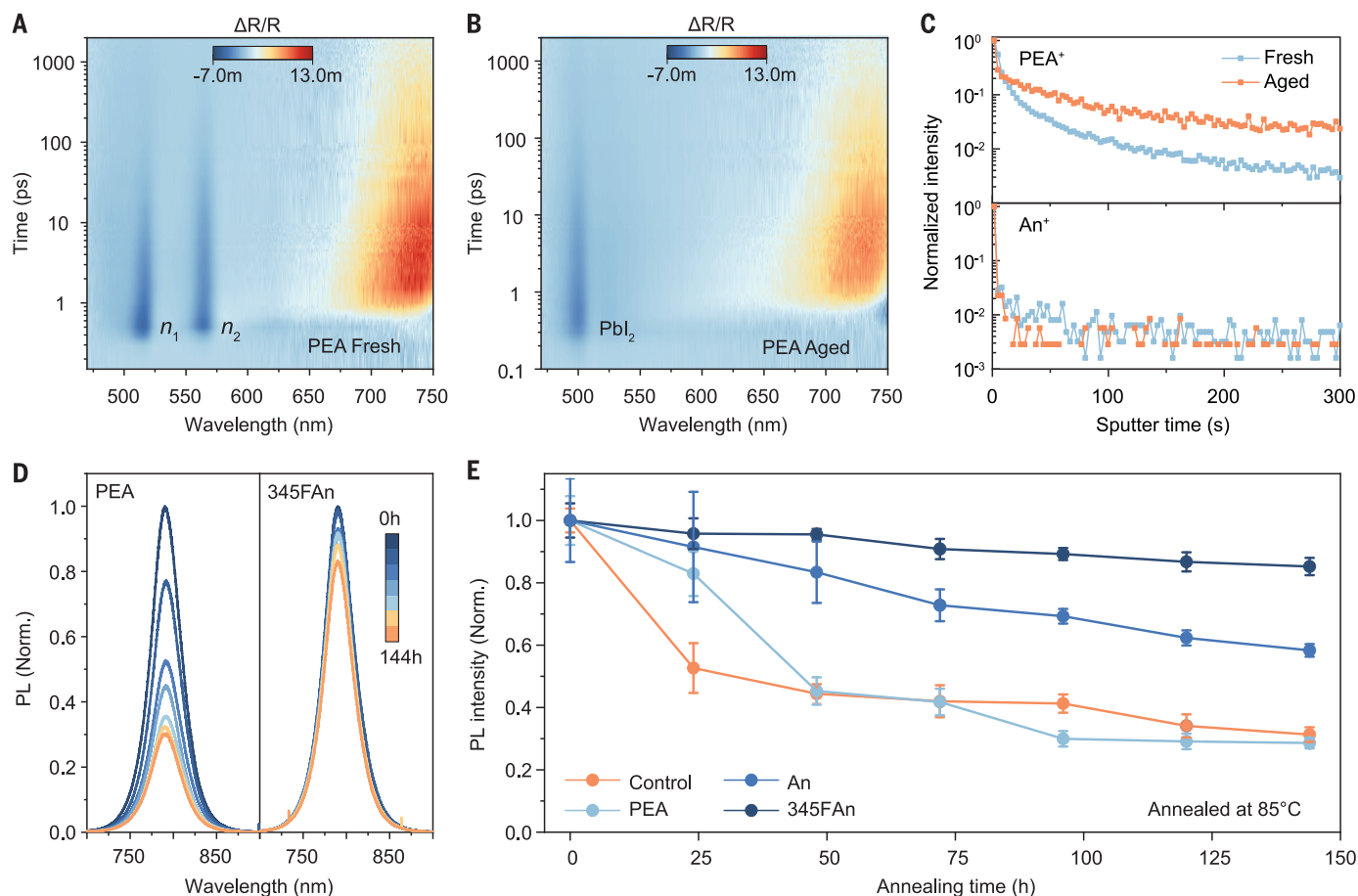
Fig. 4. Thermal stability of perovskite films. (**A** and **B**) Pseudocolor representation of the transient reflectance spectra for PEA-treated perovskite films before (A) and after (B) thermal aging at 85°C for 2 hours. 2D perovskites were decomposed into PbI$_2$ after thermal aging. (**C**) The distribution of PEA$^+$ and An$^+$ in fresh and aged (at 85°C for 2 hours) perovskite films observed with TOF-SIMS. (**D**) PL spectra of perovskite thin films under thermal annealing at 85°C. The films were kept on a hot plate at 85°C in the N$_2$-filled glovebox and measured every 24 hours in ambient air. (**E**) Changes in PL intensity for different annealing times. Data are presented as mean values ± standard deviation. Three films were measured under each condition.

sweep (Fig. 5C and fig. S19). The QSS-certified efficiency reported for inverted PSCs is compared with that of other devices in table S2.

Seeking a better understanding of the improved performance, we used ultraviolet photoelectron spectroscopy (UPS) to characterize the electronic structure of the perovskite films. The secondary electron cutoff spectra (fig. S20) showed that 345FAn decreased the work function of perovskites from 4.64 to 4.17 eV and shifted the valence-band maximum from 1.15 eV below the Fermi level in the control perovskites to 1.50 eV below the Fermi level. These results show that 345FAn induced more n-type character in the perovskite film (fig. S20), which in inverted PSCs leads to favorable band bending for electron extraction and a decrease in nonradiative carrier recombination (*44, 45*).

We performed optoelectronic characterization to investigate carrier recombination. From photoluminescence quantum yield (PLQY) measurements, we identified nonradiative recombination at the perovskite/C$_{60}$ interface as the limiting factor for the performance of control

devices (fig. S21). This recombination loss corresponded to a reduction of the quasi-Fermi level splitting (QFLS) by ~100 meV (table S3) (*46, 47*). We found that PEA and 345FAn passivation could reduce the interfacial nonradiative recombination, as reflected by the improved QFLS relative to the control stack, by ~15 and ~30 meV, respectively. We further analyzed the energy loss of PSCs on the basis of the device diode characteristics (figs. S22 and S23) (*48*). Consistent with the PL studies, nonradiative losses were reduced for PEA and 345FAn devices (12.7 and 12.1% for PEA and 345FAn, respectively) compared with those of the control device (16.5%) (fig. S24).

We evaluated the effect of ligand reactivity on the material processing of PSCs. We varied the solution exposure time between 0 s (dynamic spinning) and 120 s and tracked the PV parameters of PSCs accordingly (Fig. 5D and fig. S25). The average PCE of PEA devices (eight devices for each condition) dropped to 15.8%, with an average fill factor (FF) of merely 67.4% over the course of solution exposure for 30 s,

whereas 345FAn devices maintained an average PCE of 23.0% (Fig. 5D). Wide solution-processing windows were also achieved for other non-penetrating ligands, such as 35tbuAn, 4FAn, and 26FAn (fig. S26). In pursuit of initial evidence of capacity to scale area, we fabricated perovskite solar modules (PSMs) with an active area of 22 cm^2 and nine interconnected subcells (materials and methods). The champion PCE under reverse voltage scan was improved from 19.9 to 20.8% for the 345FAn-treated PSMs, with an open-circuit voltage (V_{oc}) of 10.13 V, an FF of 74.2%, and a J_{sc} of 2.77 mA cm^{-2} (fig. S27).

We studied the operating stability of PSCs using ISOS protocols (*49*). Accelerated lifetime testing was performed at the ISOS-L-3-85°C level, constituting light-soaking tests at 50% RH and 85°C with MPP tracking. We used atomic-layer deposition for SnO$_2$ as the buffer layer and Cs$_{0.05}$MA$_{0.05}$FA$_{0.9}$Pb(I$_{0.95}$Br$_{0.05}$)$_3$ perovskites as the absorber (materials and methods). The initial PCEs of the encapsulated control, PEA, and 345FAn devices were 18.9, 20.1, and 20.2%, respectively (fig. S28). The stability
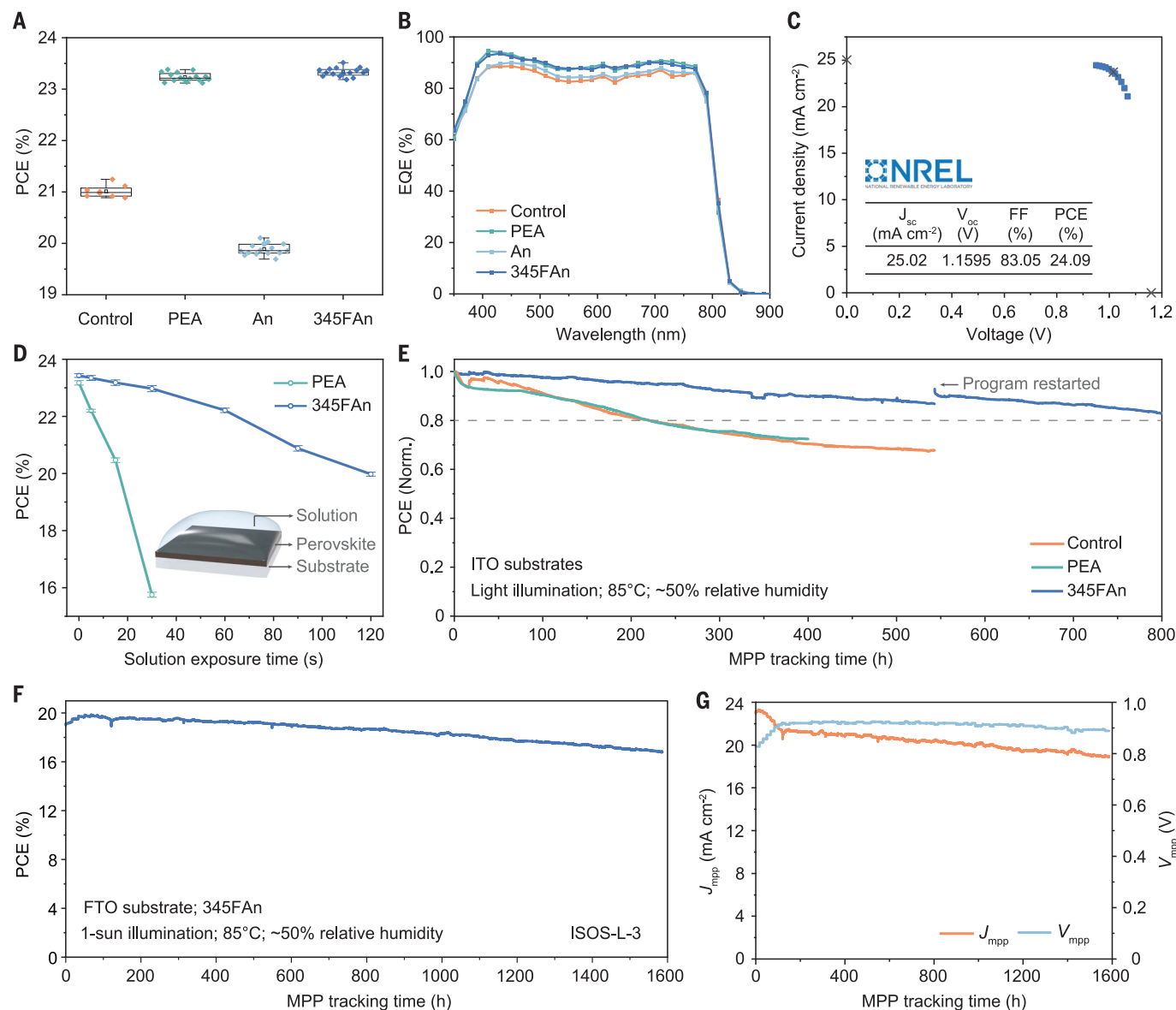
Fig. 5. Photovoltaic performance of PSCs with interface engineering.
(**A**) PCE for control (8 devices) versus ammonium ligand–treated (16 devices for each type) PSCs. (**B**) EQE curves of the control and ammonium ligand–treated devices. (**C**) QSS current density-voltage (*J-V*) curve of one representative 345FAn device certified at NREL. (Inset) PV parameters of the device. (**D**) PCE evolution of PEA and 345FAn devices as a function of solution exposure time (8 devices for each condition). Data are presented as mean values ± standard deviation. (Inset) Schematic illustration of the solution exposure process for interface engineering. (**E**) MPP tracking of encapsulated control, PEA, and 345FAn devices performed using ITO substrates at 85°C with an RH of ~50% under 0.8-sun illumination. (**F** and **G**) PCE (F), current density (J_{mpp}), and voltage (V_{mpp}) (G) at the MPP of the encapsulated 345FAn device determined using an FTO substrate under 1-sun illumination at 85°C and ~50% RH.

results are shown in Fig. 5E. We recorded a similar T_{80} of ~220 hours for the control and PEA devices, in accordance with the limited thermal stability of perovskite films (Fig. 3E). We found that 2D/3D PSCs based on alkyl ammonium BA and OA were even less stable than the control device (fig. S29). By contrast, the 345FAn device retained >80% of its initial value after the 800-hour test. We estimate the T_{80} for the 345FAn device to be ~810 hours (fig. S30), representing a fourfold enhancement over the operating lifetime of the PEA device.

To improve the T_{80} further, we moved to fluorine-doped tin oxide (FTO) as an alternative transparent electrode (fig. S31) because of its chemical stability (*50, 51*). We monitored the MPP of the encapsulated device under 1-sun illumination at 50% RH and 85°C. The initial PCE was 19.0%, which increased progressively to a peak value of 19.9% after ~50 hours of operation (Fig. 5F). This maximum PCE (PCE$_{max}$) corresponds to a temperature coefficient of −0.12% /°C relative to the room temperature device PCE (21.5%), which is con-

sistent with reported results for inverted PSCs (*52*). After 1586 hours of continuous operation, the PCE dropped to 16.8% (84% of the PCE$_{max}$), primarily because of a reduction in current density (Fig. 5G). We determined the T_{85} to be ~1560 hours (Fig. 5F). A comparison with other ISOS-L-3-stable PSCs is provided in table S4.

Discussion

Two types of 2D/3D heterostructures have been reported for ISOS-L-3-stable PSCs: 3FPEA-intercalated 2D/3D perovskites (*23*) and

all-inorganic heterostructures (*12*). For all-inorganic PSCs, the T_{85} reached an impressive 4000 hours at 85°C, but with further room for progress in PCE (≤17% when measured at 85°C). 3FPEA-based PSCs have achieved PCEs exceeding 23% at room temperature, but stable operation over 500 hours was limited to 65°C.

Aided by spectroscopic techniques, including AR-XPS, TOF-SIMS, and TR, we see evidence here that certain 2D/3D heterostructures, such as those employing typical ammonium ligands including PEA, 3FPEA, BA, and OA, may evince thermal degradation, something we assign to the dynamic nature of the interfaces at elevated temperatures. Anilinium and its fluorinated derivatives offer a more robust interface structure correlated with limited penetration into the bulk of perovskites. Fluorinated An contributes interface passivation linked to strong interactions with perovskite surfaces. The resultant optimized 345FAn devices are among the most stable PSCs seen under ISOS-L-3 protocols at 85°C, achieving PCE of 19.9% during MPP tracking at this elevated operating temperature.

REFERENCES AND NOTES

1. N. M. Haegel et al., Science **364**, 836–838 (2019).
2. National Renewable Energy Laboratory, Best research-cell efficiency chart, revised 26 May 2023; https://www.nrel.gov/pv/cell-efficiency.html.
3. H. Min et al., Nature **598**, 444–450 (2021).
4. M. Kim et al., Science **375**, 302–306 (2022).
5. J. Jeong et al., Nature **592**, 381–385 (2021).
6. Z. Song et al., Energy Environ. Sci. **10**, 1297–1305 (2017).
7. Y. Zhao et al., Nat. Energy **7**, 144–152 (2022).
8. S. Bai et al., Nature **571**, 245–250 (2019).
9. Q. Cao et al., Sci. Adv. **7**, eabg0633 (2021).
10. Y. Liu et al., Angew. Chem. Int. Ed. **59**, 15688–15694 (2020).
11. Y.-H. Lin et al., Science **369**, 96–102 (2020).
12. X. Zhao et al., Science **377**, 307–310 (2022).
13. R. Lin et al., Nature **603**, 73–78 (2022).
14. X. Li et al., Science **375**, 434–437 (2022).
15. L. Chao et al., Research **2020**, 2616345 (2020).
16. H. Kim et al., Nat. Commun. **11**, 3378 (2020).
17. H. Zhu et al., Adv. Mater. **32**, 1907757 (2020).
18. S. Yang et al., Science **365**, 473–478 (2019).
19. J. Warby et al., Adv. Energy Mater. **12**, 2103567 (2022).
20. S. M. Park, A. Abtahi, A. M. Boehm, K. R. Graham, ACS Energy Lett. **5**, 799–806 (2020).
21. J. J. Yoo et al., Energy Environ. Sci. **12**, 2192–2199 (2019).
22. J. J. Yoo et al., Nature **590**, 587–593 (2021).
23. H. Chen et al., Nat. Photonics **16**, 352–358 (2022).
24. A. H. Proppe et al., Nat. Commun. **12**, 3472 (2021).
25. S. Sidhik et al., Science **377**, 1425–1430 (2022).
26. Y. Liu et al., Sci. Adv. **5**, eaaw2543 (2019).
27. J. Chakkamalayath, N. Hiott, P. V. Kamat, ACS Energy Lett. **8**, 169–171 (2023).
28. C. A. R. Perini et al., Adv. Mater. **34**, 2204726 (2022).
29. A. A. Sutanto et al., Nano Lett. **20**, 3992–3998 (2020).
30. R. Azmi et al., Science **376**, 73–77 (2022).
31. Q. Jiang et al., Nat. Photonics **13**, 460–466 (2019).
32. C. Liu et al., Nat. Commun. **12**, 6394 (2021).
33. S. Kumar, L. Houben, K. Rechav, D. Cahen, Proc. Natl. Acad. Sci. U.S.A. **119**, e2114740119 (2022).
34. M. M. Tavakoli et al., Energy Environ. Sci. **11**, 3310–3320 (2018).
35. S.-H. Lee et al., ACS Energy Lett. **6**, 1612–1621 (2021).
36. C. S. Fadley, Prog. Surf. Sci. **16**, 275–388 (1984).
37. B. Lv, T. Qian, H. Ding, Nat. Rev. Phys. **1**, 609–626 (2019).
38. Y. Wei et al., Adv. Energy Mater. **9**, 1900612 (2019).
39. D. Bi et al., Nat. Commun. **9**, 4482 (2018).
40. H. Zhu et al., J. Am. Chem. Soc. **143**, 3231–3237 (2021).
41. M. A. Hope et al., J. Am. Chem. Soc. **143**, 1529–1538 (2021).
42. Y. Yang et al., Nat. Energy **2**, 16207 (2017).
43. R. Lyu, C. E. Moore, T. Liu, Y. Yu, Y. Wu, J. Am. Chem. Soc. **143**, 12766–12776 (2021).
44. D. Luo et al., Science **360**, 1442–1446 (2018).
45. Q. Jiang et al., Nature **611**, 278–283 (2022).
46. M. Stolterfoht et al., Adv. Mater. **32**, 2000080 (2020).
47. M. Stolterfoht et al., Nat. Energy **3**, 847–854 (2018).
48. H. Zhang et al., Nat. Commun. **12**, 3383 (2021).
49. M. V. Khenkin et al., Nat. Energy **5**, 35–49 (2020).
50. J. D. Benck, B. A. Pinaud, Y. Gorlin, T. F. Jaramillo, PLOS ONE **9**, e107942 (2014).
51. R. A. Kerner, B. P. Rand, ACS Appl. Energy Mater. **2**, 6097–6101 (2019).
52. T. Moot et al., ACS Energy Lett. **6**, 2038–2047 (2021).